CrossMark

Evidence for TiO in the Atmosphere of the Hot Jupiter HAT-P-65 b

Guo Chen[1,2] , Enric Pallé[3,4] , Hannu Parviainen[3,4] , Felipe Murgas[3,4] , and Fei Yan[5]

[1] CAS Key Laboratory of Planetary Sciences, Purple Mountain Observatory, Chinese Academy of Sciences, Nanjing 210023, People's Republic of China
guochen@pmo.ac.cn
[2] CAS Center for Excellence in Comparative Planetology, Hefei 230026, People's Republic of China
[3] Instituto de Astrofísica de Canarias, Vía Láctea s/n, E-38205 La Laguna, Tenerife, Spain
[4] Departamento de Astrofísica, Universidad de La Laguna, E-38206 La Laguna, Tenerife, Spain
[5] Institut für Astrophysik, Georg-August-Universität, Friedrich-Hund-Platz 1, D-37077 Göttingen, Germany
Received 2020 December 11; revised 2021 April 22; accepted 2021 April 26; published 2021 May 25

Abstract

We present the low-resolution transmission spectra of the puffy hot Jupiter HAT-P-65b ($0.53\,M_{Jup}$, $1.89\,R_{Jup}$, $T_{eq} = 1930\,K$), based on two transits observed using the OSIRIS spectrograph on the 10.4 m Gran Telescopio CANARIAS. The transmission spectra of the two nights are consistent, covering the wavelength range 517–938 nm and consisting of mostly 5 nm spectral bins. We perform equilibrium-chemistry spectral retrieval analyses on the jointly fitted transmission spectrum and obtain an equilibrium temperature of 1645^{+255}_{-244} K and a cloud coverage of $36^{+23}_{-17}\%$, revealing a relatively clear planetary atmosphere. Based on free-chemistry retrieval, we report strong evidence for titanium oxide (TiO). Additional individual analyses in each night reveal weak-to-moderate evidence for TiO in both nights, but moderate evidence for Na or VO only in one of the nights. Future high-resolution Doppler spectroscopy as well as emission observations will help confirm the presence of TiO and constrain its role in shaping the vertical thermal structure of HAT-P-65b's atmosphere.

1. Introduction

Titanium and vanadium oxides (TiOs and VOs) exhibit prominent molecular absorption bands in the optical spectra of M dwarfs, and their signatures gradually disappear in cooler L dwarfs ($T_{eff} \sim 1700$–$1900\,K$; Kirkpatrick et al. 1999). Similarly, TiO and VO have long been expected to be the dominant opacity sources in the atmospheres of highly irradiated hot Jupiters and responsible for causing thermal inversions (Hubeny et al. 2003; Fortney et al. 2008).

Up until now, thermal inversions have been detected in the dayside of several ultra-hot Jupiters using low-resolution emission observations (e.g., Haynes et al. 2015; Evans et al. 2017; Sheppard et al. 2017; Arcangeli et al. 2018; Mansfield et al. 2018). Recent high-resolution Doppler emission spectroscopy observations (Pino et al. 2020; Yan et al. 2020; Nugroho et al. 2020) reveal that these inversions are at least partly induced by optical absorbers such as atomic Fe or Mg lines or continuum H^-, regardless of the presence of TiO or VO (Lothringer et al. 2018).

Indeed, TiO and VO have been rarely detected. The most confident detection of TiO comes from the atmosphere of WASP-33b with high-resolution Doppler emission spectroscopy (Nugroho et al. 2017; but also see Herman et al. 2020; Serindag et al. 2021). Sedaghati et al. (2017) reported a detection of TiO in the low-resolution transmission spectrum of WASP-19b, while Espinoza et al. (2019) reported a nondetection based on independent observations. Tentative evidence of TiO/VO was also claimed in the low-resolution transmission spectrum of WASP-121b (Evans et al. 2016, 2018), but later Merritt et al. (2020) reported nondetections for both TiO and VO using high-resolution Doppler transmission spectroscopy. Thus, the existence and detectability of TiO/VO in hot-Jupiter atmospheres remain an open question.

Here, we report strong evidence for TiO in the atmosphere of the hot Jupiter HAT-P-65b using low-resolution transmission spectroscopy. HAT-P-65b is a very puffy hot Jupiter ($0.53\,M_{Jup}$, $1.89\,R_{Jup}$) orbiting a G2 star every 2.61 days (Hartman et al. 2016). With an equilibrium temperature of $1930 \pm 45\,K$, it falls near the transition regime where ultra-hot Jupiters are defined (e.g., $T_{eq} > 2000\,K$; Lothringer et al. 2018). In Section 2, we summarize the observations and data reduction. We then describe the light-curve analysis in Section 3 and interpret the transmission spectrum in Section 4. Finally, we give the summary and discuss its implications in Section 5.

2. Observations and Data Reduction

We observed two transits of HAT-P-65b under the programs GTCMULTIPLE2C-18A (PI: G. Chen) and GTC24-20A (PI: E. Pallé) using the OSIRIS spectrograph (Cepa et al. 2000) installed on the 10.4 m Gran Telescopio CANARIAS (GTC) in La Palma, Spain. OSIRIS is equipped with two CCDs to cover the unvignetted field of view of $\sim 7'.5$. In both observations, OSIRIS was configured in the long-slit mode with a $12''$ slit. The target star HAT-P-65 ($r' = 12.95$ mag) and the reference star 2MASS J21034527 + 1158213 ($r' = 12.88$ mag, $2'.19$ away) were both located on CCD 1 and simultaneously placed in the slit. The 200 kHz readout and 2×2 binning ($0''.254$ per binned pixel) were adopted. The R1000R grism was used to acquire the spectra, covering a wavelength range of 510–1000 nm at a dispersion of $\sim 2.6\,\text{Å}$ per binned pixel. The HeAr, Ne, and Xr arc lamps were observed through a $1''.23$ slit.

The two transits were observed on the nights of 2018 July 29 (Night 1) and 2020 August 7 (Night 2), covering UT windows of 21:27–05:41 and 21:08–04:05, respectively. The typical seeing was $\sim 0''.9$ for Night 1 and $\sim 0''.6$ for Night 2. To avoid saturation, a slight defocusing was used in both nights, increasing the FWHMs of the point-spread function (PSF) in
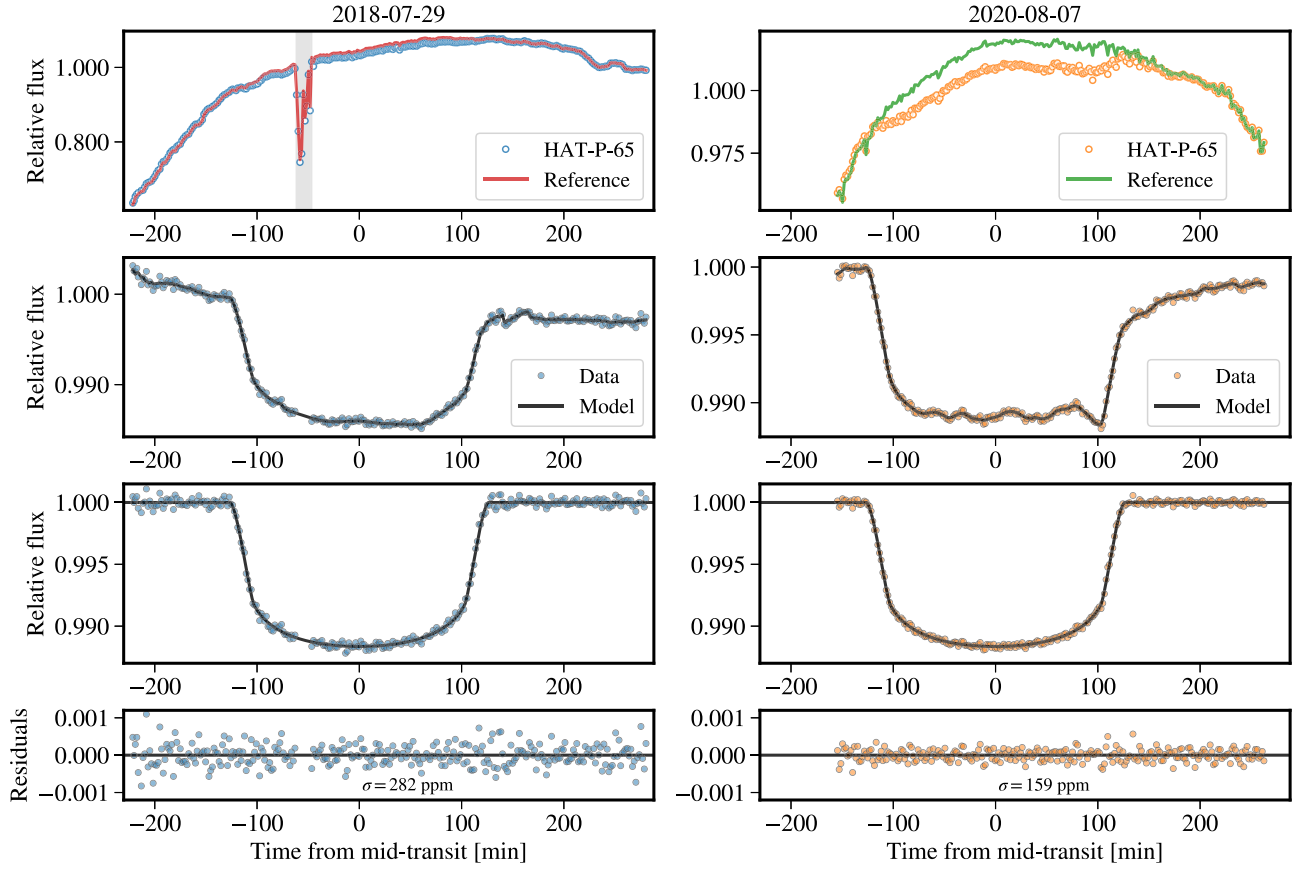
Figure 1. White light curves of HAT-P-65b observed by GTC/OSIRIS on the nights of 2018 July 29 (left, Night 1) and 2020 August 7 (right, Night 2). From top to bottom are (i) raw flux time series of HAT-P-65 and its reference star, (ii) raw white light curves of HAT-P-65 (i.e., normalized target-to-reference flux ratios), (iii) white light curves corrected for systematics, and (iv) best-fit light-curve residuals. The best-fit models are shown in black.

the cross-dispersion direction to median values of $\sim 1\rlap{.}''3$ (Night 1) and $\sim 1\rlap{.}''0$ (Night 2). An exposure time of 75 s was used for both nights, resulting in 305 and 255 spectra for the first and second nights, respectively. For Night 1, there was a thin cirrus crossing event after the ingress ended. Nine spectra acquired during that time were discarded.

We reduced the raw data using the methodology adopted in our previous studies (e.g., Chen et al. 2018, 2020a). The spectral images were corrected for overscan, bias, flat, sky background, and cosmic rays. The one-dimensional spectra were extracted using an aperture radius of 9 pixels (Night 1) and 8 pixels (Night 2). The aperture radius was optimized by minimizing the point-to-point scatter in the white light curves. We note that there is a faint background companion star at $\sim 3\rlap{.}''6$, but contributing negligible flux within the chosen apertures (see Appendix A). The initial wavelength solution was constructed by the arc lines, which was later revised to allow that all the spectra of the target and reference stars were well aligned in the wavelength domain. The time stamp was created in Barycentric Julian Dates in Barycentric Dynamical Time (BJD$_{\mathrm{TDB}}$; Eastman et al. 2010).

We created the white light curves by summing the flux within the wavelength range 514–908 nm, but excluding the 754–768 nm region to avoid the telluric oxygen A-band. To create the spectroscopic light curves, we divided the spectra

Table 1
Parameters Derived from White Light Curves

Parameter	Prior	Posterior Estimate
P [d]	2.6054552(fixed)	⋯
i [°]	$\mathcal{U}(80, 90)$	$89.10^{+0.63}_{-0.83}$
$a/R_\star$	$\mathcal{U}(2, 8)$	$5.221^{+0.025}_{-0.043}$
$R_\mathrm{p}/R_\star$	$\mathcal{U}(0.05, 0.15)$	$0.0994^{+0.0025}_{-0.0025}$
u_1	$\mathcal{N}(0.356, 0.045^2)$	$0.333^{+0.037}_{-0.038}$
u_2	$\mathcal{N}(0.277, 0.027^2)$	$0.270^{+0.026}_{-0.025}$
	2018-07-29: Night 1	
T_mid [MJD[a]]	$\mathcal{U}(8329.53, 8329.57)$	$8329.54828^{+0.00029}_{-0.00029}$
σ_w [10^{-6}]	$\mathcal{U}(0.1, 5000)$	284^{+16}_{-15}
$\ln A$	$\mathcal{U}(-10, -1)$	$-6.41^{+0.36}_{-0.28}$
$\ln \tau_t$	$\mathcal{U}(-6, 6)$	$-2.52^{+0.33}_{-0.29}$
$\ln \tau_x$	$\mathcal{U}(-6, 6)$	$1.64^{+0.41}_{-0.35}$
	2020-08-07: Night 2	
T_mid [MJD[a]]	$\mathcal{U}(9069.48, 9069.52)$	$9069.49472^{+0.00034}_{-0.00034}$
σ_w [10^{-6}]	$\mathcal{U}(0.1, 5000)$	147^{+12}_{-12}
$\ln A$	$\mathcal{U}(-10, -1)$	$-6.74^{+0.33}_{-0.24}$
$\ln \tau_t$	$\mathcal{U}(-6, 6)$	$-3.32^{+0.27}_{-0.23}$
$\ln \tau_x$	$\mathcal{U}(-6, 6)$	$3.52^{+1.39}_{-0.84}$

[a] MJD = BJD$_{\mathrm{TDB}}$ − 2450000.
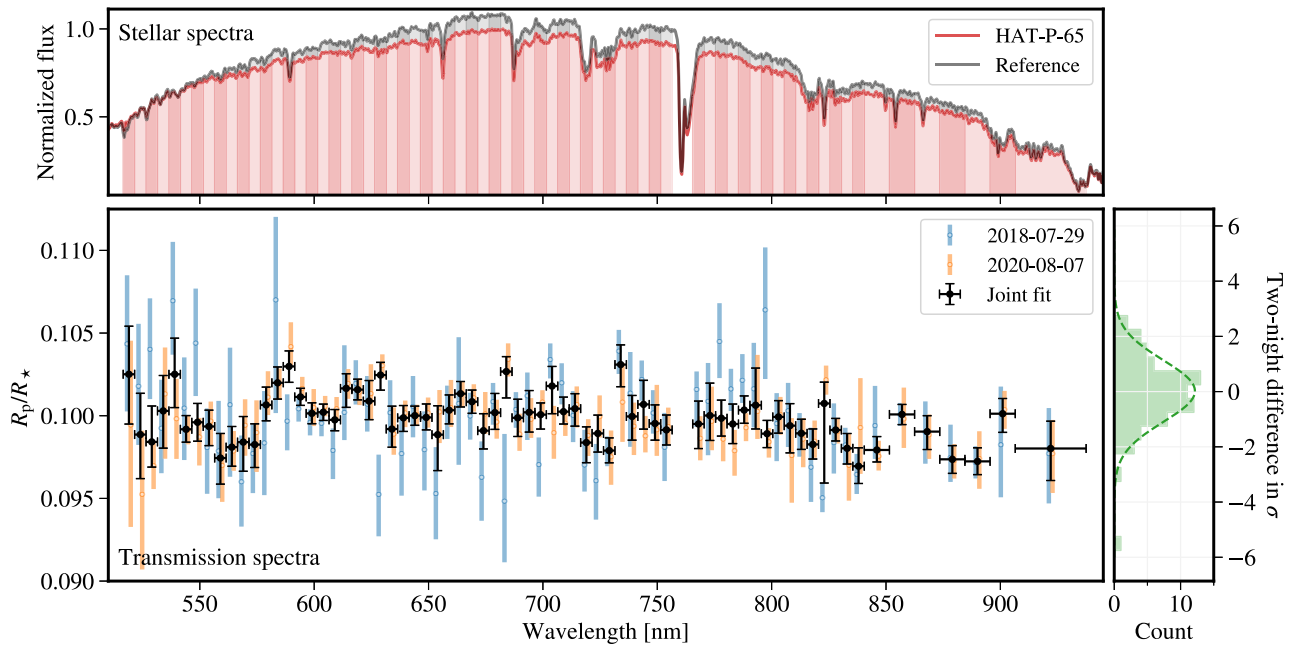
Figure 2. Transmission spectra of HAT-P-65b measured jointly (black) and individually (blue and orange) for the two nights. The top subpanel shows an example of the stellar spectra for HAT-P-65 and its reference star, along with the passbands used in this work marked in shaded colors. The right subpanel presents the distribution histogram of the two-night differences, which has been normalized by the measurement uncertainties.

into 63 channels of 5 nm bin, 6 channels of 11 nm bin, and 1 channel of 31 nm bin. We set up broader bins at longer wavelengths due to the appearance of a fringing pattern at $\lambda \gtrsim 830$ nm.

3. Light-curve Analysis

We modeled the white and spectroscopic light curves following the approach described in Chen et al. (2018, 2020a). Here we first give a summary of general procedures, and then present the specifics in the subsections.

The light curves were assumed to consist of astrophysical signals and correlated systematics. The transit was described by the Mandel & Agol (2002) model, implemented via the Python package batman (Kreidberg 2015) and parameterized by orbital period P (fixed to 2.6054552 d; Hartman et al. 2016), orbital inclination i, scaled semimajor axis $a/R_\star$, radius ratio $R_p/R_\star$, mid-transit time T_{mid}, and limb-darkening coefficients u_i. A circular orbit was adopted (Hartman et al. 2016). The correlated systematics were treated as Gaussian processes (GPs; Rasmussen & Williams 2006; Gibson et al. 2012), implemented via the Python package george (Ambikasaran et al. 2015).

The quadratic limb-darkening law was adopted, and the coefficients u_1 and u_2 were fitted with Gaussian priors. The priors were calculated using the Kurucz ATLAS9 stellar atmosphere models by a Python code from Espinoza & Jordán (2015). The grid with stellar effective temperature $T_{eff} = 5750$ K, surface gravity $\log g_\star = 4.0$, and metallicity [Fe/H] = 0.1 was used to derive the prior mean values, while the average differences among the grids with $T_{eff} = 5500$ K, 5750 K, and 6000 K were adopted as the prior sigma values.

To explore the marginalized posterior distributions of fitted parameters, the affine-invariant Markov Chain Monte Carlo (MCMC) was used, implemented via the Python package emcee (Foreman-Mackey et al. 2013). The walkers are initialized around literature values for transit parameters and arbitrary values for others. The number of walkers are set to be at least twice the number of free parameters (50 and 32 for the white and spectroscopic light curves, respectively). We always run two short chains (1000 steps) for the "burn-in" phase and then start a long chain (20,000 steps) for the posterior estimation. The chain length is kept to be more than 50 times autocorrelation time to ensure convergence.

3.1. White Light Curves

The white light curves of the two nights were jointly fitted, sharing the same values for (i, $a/R_\star$, $R_p/R_\star$, u_1, u_2). The transit model was adopted as the GP mean function, while the Matérn $\nu = 3/2$ kernel

$$k_{ij} = A^2 (1 + \sqrt{3 D_{ij}^2}) \exp(-\sqrt{3 D_{ij}^2}) \qquad (1)$$

was adopted as the GP covariance matrix, where $D_{ij}^2 = \sum_{\alpha=1}^{N} (\hat{x}_{\alpha,i} - \hat{x}_{\alpha,j})^2 / \tau_\alpha^2$, and A and τ_α are the characteristic correlation amplitude and length scale. We chose time t and spectral drift x as the GP covariance matrix inputs (see Appendix B for model selection details). In the light-curve modeling, uniform priors were adopted for (i, $a/R_\star$, $R_p/R_\star$, T_{mid}, σ_w), while log-uniform priors were adopted for (A, τ_t, τ_x), where σ_w is the white noise jitter to inflate the light-curve uncertainties.

The white light curves are presented in Figure 1. The best-fit residuals have a standard deviation of 282 ppm (Night 1) and 159 ppm (Night 2), which are 2.94× and 1.63× photon noise, respectively. The derived parameters are presented in Table 1. Our transit parameters do not agree well with those reported in the discovery paper ($i = 84.2 \pm 1°.3$, $a/R_\star = 4.57 \pm 0.20$; Hartman et al. 2016). This can be probably attributed to the fact that all the follow-up observations in the discovery paper only covered partial transits.
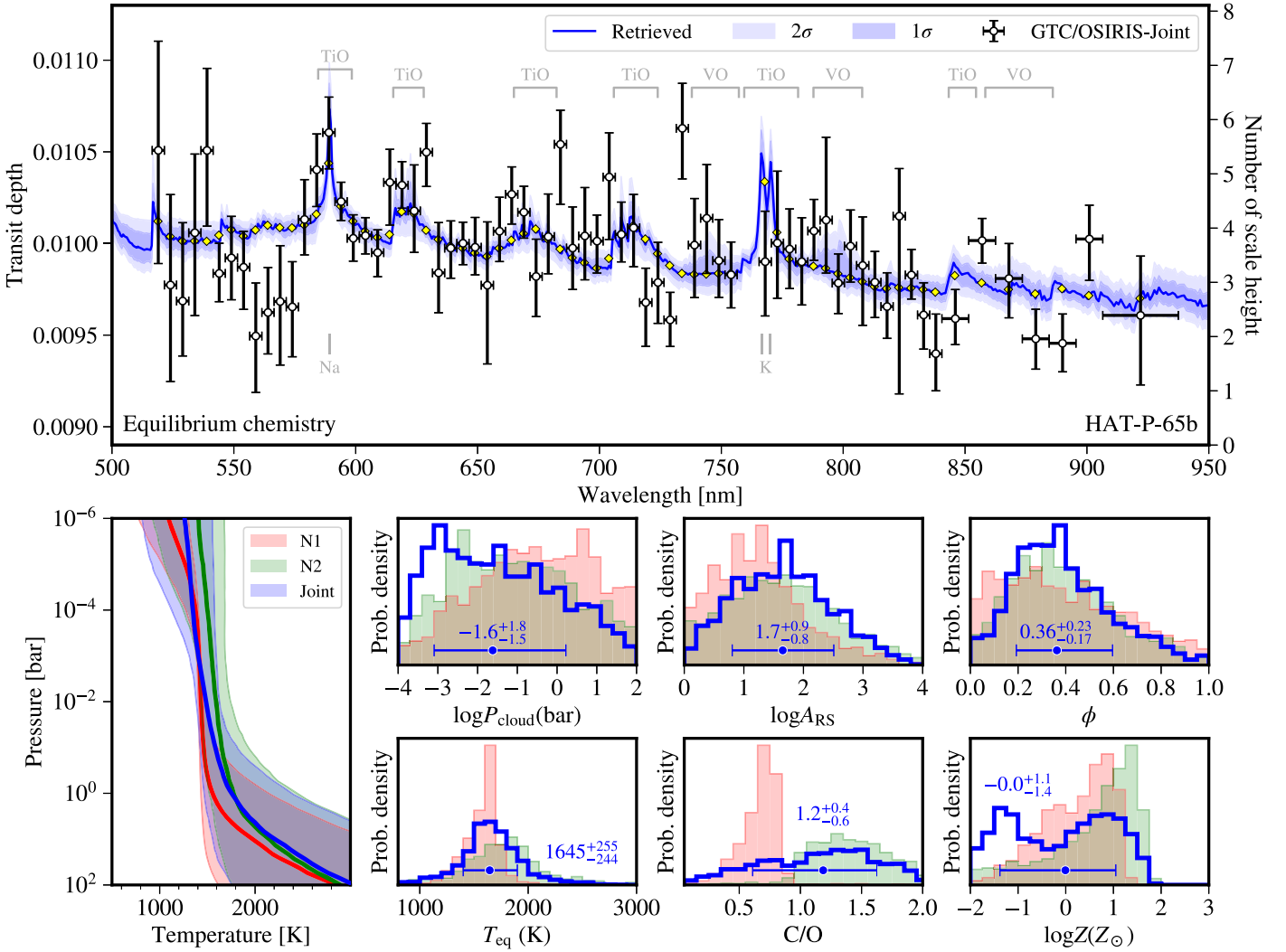
Figure 3. Transmission spectrum of HAT-P-65b and retrieved atmospheric properties assuming equilibrium chemistry. The first row presents the jointly derived transmission spectrum (white circles) and retrieved models (blue line and shaded areas). The second and third rows present the retrieved temperature–pressure (T–P) profile, cloud-top pressure $P_{\rm cloud}$, enhancement over H_2 Rayleigh scattering $A_{\rm RS}$, cloud coverage ϕ, equilibrium temperature $T_{\rm eq}$ used in the T–P profile, C/O ratio, and atmospheric metallicity Z. The blue, red, and green lines and shaded areas refer to the retrieval results based on the joint, Night 1 (N1), and Night 2 (N2) transmission spectra, respectively.

In addition to the joint analysis, we also performed the light-curve modeling for each transit individually. This resulted in $i = 88°.96^{+0.73}_{-0.99}$, $a/R_\star = 5.188^{+0.034}_{-0.059}$, and $R_p/R_\star = 0.1029^{+0.0035}_{-0.0036}$ for Night 1, and $88°.89^{+0.78}_{-1.03}$, $5.234^{+0.036}_{-0.069}$, and $0.0966^{+0.0034}_{-0.0035}$ for Night 2. While the best-fit transit depths are discrepant to some extent, the large uncertainties still make them consistent at 1.3σ. We note that the strong (but achromatic) systematics in Night 2 might have contributed to this bias.

3.2. Spectroscopic Light Curves

Before modeling the spectroscopic light curves, we first derived the empirical common-mode systematics models by dividing the white light curves by the best-fit transit model. For each night, the spectroscopic light curves were divided by the corresponding empirical models to correct for the common-mode systematics. The corrected spectroscopic light curves were then fitted in a similar way as described in the last subsection, except that the values of i, $a/R_\star$, and $T_{\rm mid}$ were fixed to the best-fit values obtained for the white light curves.

Fixing the values of i and $a/R_\star$ to Hartman et al.'s (2016) has negligible impact on the derived transmission spectrum (see Appendix C). We chose the transit model as the GP mean function and time t as the GP covariance matrix input (see Appendix B). Consequently, the free parameters were ($R_p/R_\star$, u_1, u_2, σ_w, A, τ_t).

The spectroscopic light curves of the two nights were fitted in two separate runs. In the first run, the two nights were fitted individually, so as to examine the consistency between them. In the second run, the two nights were fitted jointly, sharing the same values for ($R_p/R_\star$, u_1, u_2). In general, the spectroscopic light curves of Night 2 have better precision than Night 1. For Night 1, the standard deviation of the best-fit residuals achieve 1.3–2.1× photon noise, while for Night 2 it is 1.0–1.8× photon noise.

Figure 2 gives an illustration of the spectroscopic passbands, and presents the individually and jointly fitted transmission spectra. The two nights are consistent with each other at 1.5σ confidence level ($\chi^2 = 81.7$ for 68° of freedom, hereafter dof), after excluding two outlier channels located at 629 nm and 823 nm in which the two nights are different for more than 3σ.
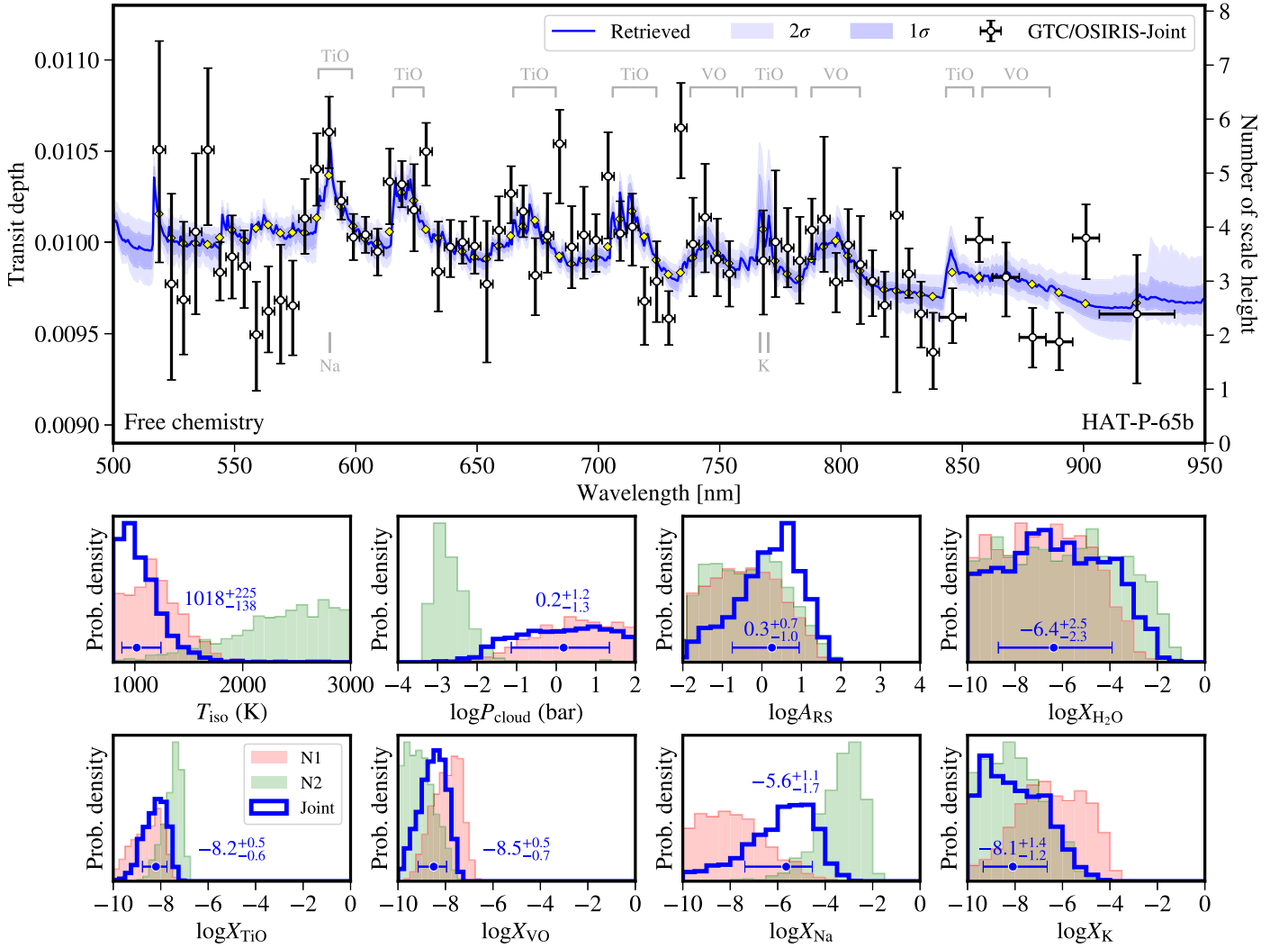
Figure 4. Transmission spectrum of HAT-P-65b and retrieved atmospheric properties assuming free chemistry. The first row presents the jointly derived transmission spectrum (white circles) and retrieved models (blue line and shaded areas). The second and third rows present the retrieved isothermal temperature T_{iso}, cloud-top pressure P_{cloud}, enhancement over H_2 Rayleigh scattering A_{RS}, and mass fractions X_i for H_2O, TiO, VO, Na, and K. The blue, red, and green lines and shaded areas refer to the retrieval results based on the joint, Night 1 (N1), and Night 2 (N2) transmission spectra, respectively.

Nevertheless, the histogram of the two-night differences follows a nearly Gaussian distribution. The derived transmission spectra are given in Table 3 in Appendix D.

4. Transmission Spectrum

The jointly fitted transmission spectrum of HAT-P-65b roughly spans five scale heights ($H/R_\star = 0.001475$, where $H = k_B T_{eq}/\mu g_p$). Two broad spectral features at ∼590 nm and ∼620 nm appear prominent.

To calculate the Bayesian evidence $\mathcal{Z}$ for the spectral retrieval analyses, we used the Python package PyMultiNest (Buchner et al. 2014), which relies on the MultiNest library (Feroz et al. 2009) and implements the multimodal nested sampling algorithm. For model comparison, we calculated the Bayes factor ($B_{10} = \mathcal{Z}_1/\mathcal{Z}_0$) and adopted the criteria of $\ln B_{10} = 1.0, 2.5, 5.0$ as the starting points of "weak," "moderate," and "strong" evidence in favor of model 1 over model 0 (Trotta 2008), respectively. To compare with literature, the Bayes factor was converted to the traditional frequentist significance (Trotta 2008; Benneke & Seager 2013),

but the number of "sigmas" does not necessarily mean a detection (Welbanks & Madhusudhan 2021).

We first compared HAT-P-65b's transmission spectrum to a flat line and a sloped line. The spectrum is inconsistent with a flat line at the 4.2σ level ($\chi^2 = 127.7$ for 69 dof). The flat and sloped lines have $\ln \mathcal{Z} = 456.23$ and 466.20, respectively, indicating that the sloped line is preferred over the flat line at 4.8σ level. The derived slope $d(R_p/R_\star)/d(\ln \lambda) = -0.00405 \pm 0.00078$ corresponds to a scattering index of $\alpha = -2.75 \pm 0.53$ if it is assumed to be induced by a power-law scattering cross section $\kappa = \kappa_0 (\lambda/\lambda_0)^\alpha$ (Lecavelier Des Etangs et al. 2008) in an atmosphere at the equilibrium temperature.

We then performed spectral retrieval analyses on the transmission spectrum using the Python packages petitRADTRANS (Mollière et al. 2019) and PyMultiNest. We adopted the modified Guillot (2010) temperature–pressure (T–P) profile (Mollière et al. 2019), which consists of six free parameters. Following MacDonald & Madhusudhan (2017), the atmosphere was assumed to be covered by clouds and hazes at a fraction of ϕ, with the rest being clear. The clouds and

hazes were parameterized as a cloud-top pressure (P_{cloud}) and an enhancement factor over nominal Rayleigh scattering (A_{RS}). The reference pressure P_0 at the planet radius $R_p = 1.89 R_J$ was a free parameter. We started from equilibrium chemistry, using two free parameters (C/O and metallicity $\log Z$) to interpolate mass fractions of H_2, He, CO, H_2O, HCN, C_2H_2, CH_4, PH_3, CO_2, NH_3, H_2S, VO, TiO, Na, K, SiO, e^-, H^-, H, and FeH in a precalculated chemical grid (Mollière et al. 2017). Collision-induced absorption of H_2–H_2 and H_2–He and Rayleigh scattering of H_2 and He were also included.

Figure 3 presents the best retrieved model ($\ln \mathcal{Z} = 475.79$, $\chi^2 = 77.9$ for 58 dof) assuming equilibrium chemistry, along with the posterior distributions of the T–P profile and atmospheric properties. This physics-motivated model is strongly favored over the flat-line (6.6σ) and sloped-line (4.8σ) models. We note that the data points at 629 nm and 734 nm contribute significantly to the resulting chi-square ($\Delta\chi^2 = 13.4$). We obtained a T–P profile that is nearly isothermal across a wide range of pressure levels. We retrieved an equilibrium temperature of 1645^{+255}_{-244} K, and a cloud coverage of $36^{+23}_{-17}\%$, which has a poorly constrained cloud-top pressure (0.8–1585 mbar) and a haze scattering amplitude that is 8–$398 \times H_2$ Rayleigh scattering. The C/O ratio and metallicity are not well constrained by current data.

We also performed the spectral retrieval analyses assuming free chemistry to search for the species responsible for the observed spectral signatures. In this case, we adopted an isothermal T–P profile and described the clouds/hazes properties using P_{cloud} and A_{RS}, without the consideration of cloudy/clear sections. We only included H_2, He, TiO, VO, Na, K, and H_2O in the full model, and set the mass fractions of the latter five as free parameters. Figure 4 shows the best retrieved model ($\ln \mathcal{Z} = 476.34$, $\chi^2 = 76.6$ for 61 dof; $\Delta\chi^2 = 14.4$ from 629 nm and 734 nm) and posterior distributions of atmospheric properties. The mass fraction posterior distributions show clear modes for TiO, VO, and Na at $\log X = -8.2^{+0.5}_{-0.6}$, $-8.5^{+0.5}_{-0.7}$, $-5.6^{+1.1}_{-1.7}$, but not for K and H_2O. We experimented with decreasing the prior limit and found that the TiO posterior remained the same while the posteriors of VO and Na exhibited tails bound by the lower prior limit. On the other hand, we removed certain species one by one and compared their Bayesian evidence to that of the full model. Removing any one of TiO, VO, or Na would decrease the Bayesian evidence by $\Delta \ln \mathcal{Z} = -5.2$, -0.9, -1.2, respectively. This indicates that the presence of TiO is strongly favored.

Since Night 2 is heavily weighted in the joint analysis due to higher precision, we performed the retrieval analyses in each night to inspect their individual constraints on the atmospheric properties. The derived parameters and statistics for all the analyses are presented in Tables 4 and 5 in Appendix D. We found weak-to-moderate evidence for TiO in both nights and the measured mass fractions were in broad agreement. In contrast, we only found moderate evidence for VO in Night 1 and moderate evidence for Na in Night 2, but no evidence for them in the other night. This is consistent with the results obtained in the joint transmission spectrum, highlighting the importance to conduct repeated observations to improve the credibility of any detections.

Finally, we investigated the impact of stellar heterogeneity by adding contamination of spots and faculae to the free-chemistry retrieval analyses. We included the component of stellar contamination in a way similar to Chen et al. (2021). For both individual and joint transmission spectra, the Bayesian evidence decreases significantly if no planetary atmosphere is considered, indicating that the spots/faculae alone cannot explain our observations. The retrieved planetary atmospheric properties remain consistent with those obtained in the case when no spots/faculae are included (see Figure 7 in Appendix D), except for Na mass fraction, which increases from $\log X = -5.6^{+1.1}_{-1.7}$ to $-2.5^{+1.3}_{-1.5}$. On the other hand, the Bayes factors disfavor stellar contaminations in the retrievals for Night 1 and joint transmission spectra, but not for Night 2. However, we confirm that even if stellar contamination exists in Night 2, it does not contribute any spectral signatures mimicking TiO in the case of HAT-P-65 (see Figure 8 in Appendix D).

5. Summary and Discussion

We observed two transits of HAT-P-65b using the OSIRIS spectrograph on the 10.4 m GTC, and derived two consistent individual transmission spectra. We then jointly fitted the two nights to derive the final transmission spectrum, in which at least two of the TiO absorption bands were clearly resolved (i.e., ∼585–598 nm and ∼615–628 nm). We performed spectral retrieval analyses on the joint transmission spectrum and found a relatively clear atmosphere showing strong evidence for TiO. The analyses on the individual transmission spectra instead reveal weak-to-moderate evidence for TiO in both nights, but only moderate evidence for VO or Na in one of the nights (no evidence in the other).

The detection of TiO in transmission spectroscopy is still rare and intriguing. Several mechanisms have been proposed to explain the lack of TiO detection, such as cold trapping either in deeper atmosphere or on cooler nightside (Hubeny et al. 2003; Spiegel et al. 2009; Parmentier et al. 2013), photo-dissociation (Knutson et al. 2010), or thermal dissociation (Lothringer et al. 2018; Parmentier et al. 2018). The strong evidence for TiO suggests that these mechanisms have not completely removed TiO from HAT-P-65b's observable atmosphere.

The presence of TiO in the upper atmosphere could absorb incoming stellar radiation and introduce a thermal inversion in the T–P profile (Hubeny et al. 2003; Fortney et al. 2008). We have retrieved a nearly isothermal T–P profile for the atmosphere at the day–night terminator. Given the equilibrium temperature of ∼1930 K, it is likely that HAT-P-65b's dayside temperature is not sufficiently hot to thermally dissociate TiO. Therefore, it is possible to look for the TiO signature in follow-up secondary-eclipse observations and to investigate its role in changing the vertical thermal structure.

We note that it is difficult to claim the detection of either TiO, VO, or Na at this stage. In particular, the Na line overlaps with the TiO band at ∼585–598 nm, which are difficult for low-resolution transmission spectroscopy to resolve. Fortunately, high-resolution Doppler spectroscopy, acquired using state-of-the-art ultrastable spectrographs like ESPRESSO (e.g., Ehrenreich et al. 2020; Chen et al. 2020b; Casasayas-Barris et al. 2021), will likely be able to unambiguously distinguish different atomic and molecular species and possibly their morning–evening differences, which will strongly improve our understanding of atmospheric circulation in hot Jupiters.

Appendix A
Impact of Flux Dilution by a Companion Star

Hartman et al. (2016) resolved a background companion star to HAT-P-65 with a similar effective temperature at a distance of $3\rlap{.}{''}6$ ($\Delta J = 4.91 \pm 0.01$ mag and $\Delta K = 4.95 \pm 0.03$). This companion star is also resolved in our GTC/OSIRIS observation, with a projected distance of 13.13 pixels ($3\rlap{.}{''}34$) along the slit. We adopted an aperture radius of 9 pixels ($2\rlap{.}{''}29$) and 8 pixels ($2\rlap{.}{''}03$) in the spectral extraction. To quantitatively assess the impact of the dilution of the companion star, we fitted the PSF of HAT-P-65 and its companion following the methodology described in Chen et al. (2021). We used the out-of-transit spectra images to calculate the fully integrated companion-to-target flux ratio spectrum, and recorded the standard deviation as its uncertainties. Similarly, we also calculated the flux-ratio spectrum within the aperture that was used to extract the spectra of HAT-P-65. We fitted the integrated flux-ratio spectrum using the spectral templates from the PHOENIX stellar atmospheres (Husser et al. 2013). This resulted in the stellar parameters $T_{\rm eff} = 5443^{+18}_{-14}$ K, $\log g = 3.11^{+0.17}_{-0.11}$, and $[{\rm Fe/H}] = -0.11^{+0.21}_{-0.08}$ for the companion star, with a flux rescaling factor of $f = 0.01289^{+0.00020}_{-0.00034}$ and $T_{\rm eff} = 5835$ K, $\log g = 4.18$, $[{\rm Fe/H}] = 0.10$ being fixed for HAT-P-65. In Figure 5, we present the integrated and in-aperture flux-ratio measurements. The dilution caused by the in-aperture companion flux is almost negligible. Even if the companion were fully included in the aperture (i.e., the integrated spectrum), the wavelength-dependent dilution difference is too small to explain any spectral signatures observed in the transmission spectrum. Therefore, we conclude that this companion star does not impact our results.
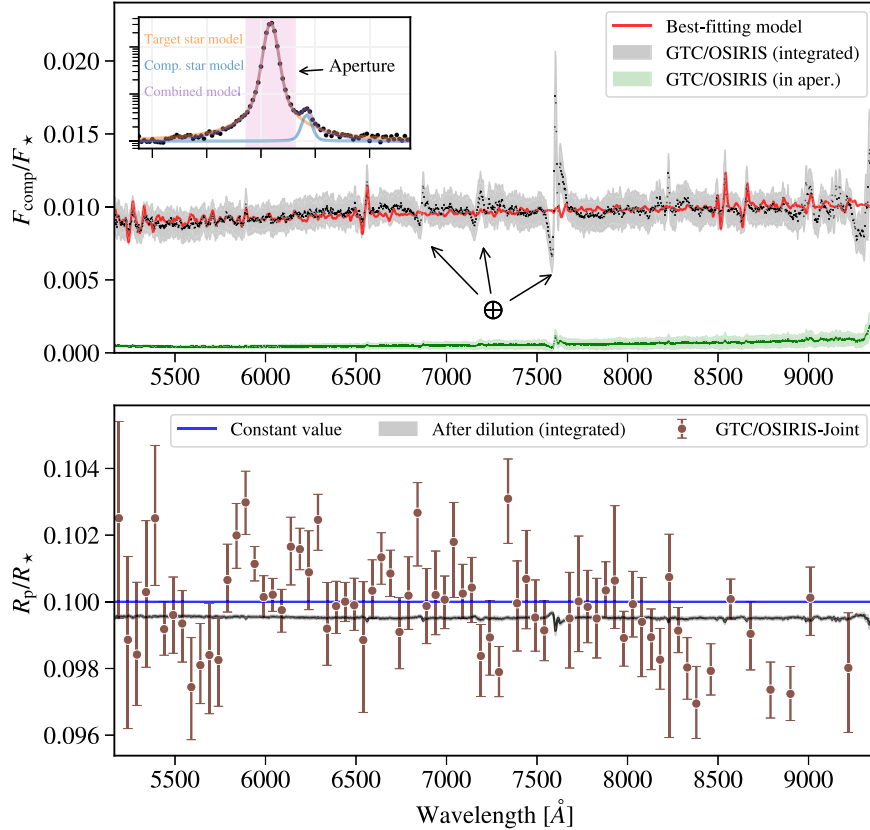
Figure 5. Top: fully integrated (black) and in-aperture companion-to-target flux-ratio spectra. The red line shows the best-fit flux-ratio model. The inset illustrates the PSF fitting for HAT-P-65 and its companion star. The pink area indicates the aperture adopted in Night 1. Bottom: dilution effect compared to joint transmission spectrum. The blue line shows a constant value (0.1000), and the black line and shaded areas correspond to the values after being diluted by the fully integrated flux-ratio spectrum.

Appendix B
Model Selection for Light-curve Analysis

To determine the optimal GP mean function, we experimented with the transit model, the transit multiplied by a linear trend or by a quadratic trend. For the GP covariance matrix input, we also tested different combinations of state vectors $\hat{x}_\alpha$ (e.g., time sequence t, spectral drift x, spatial drift y, spatial FWHM s_y). We used PyMultiNest to implement the multimodal nested sampling algorithm and to calculate the natural log of the Bayesian evidence (ln $\mathcal{Z}$). Table 2 lists the resulting ln $\mathcal{Z}$ for all the tested models. For the white light curves, Model 2 gives the most evidence and is significantly better than the other models ($>3\sigma$ for $\Delta \ln \mathcal{Z} > 3.15$), while Model 1 is the best for the spectroscopic light curves that have been corrected for the common-mode systematics. We note that the derived transit parameters were in general consistent even if a different model was used.

Table 2
Model Selection for Light-curve Analysis

| #	Model		White		Spectroscopic	
	GP	Trend	$\ln \mathcal{Z}$	$\Delta \ln \mathcal{Z}$	$\ln \mathcal{Z}$	$\Delta \ln \mathcal{Z}$
1	GP(t)	⋯	3615.89	−4.63	204343.95	0
2	GP(t, x)	⋯	3620.53	0	204294.21	−49.7
3	GP(t, y)	⋯	3617.38	−3.15	204337.49	−6.5
4	GP(t, s_y)	⋯	3616.49	−4.03	204301.83	−42.1
5	GP(t)	$B = c_0 + c_1 t$	3602.86	−17.66	203044.76	−1299.2
6	GP(t, x)	$B = c_0 + c_1 t$	3608.32	−12.20	202898.40	−1445.6
7	GP(t, y)	$B = c_0 + c_1 t$	3605.45	−15.08	202968.37	−1375.6
8	GP(t, s_y)	$B = c_0 + c_1 t$	3605.83	−14.69	202916.09	−1427.9
9	GP(t)	$B = c_0 + c_1 t + c_2 t^2$	3608.54	−11.98	202745.46	−1598.5
10	GP(t, x)	$B = c_0 + c_1 t + c_2 t^2$	3608.83	−11.69	202604.22	−1739.7
11	GP(t, y)	$B = c_0 + c_1 t + c_2 t^2$	3609.66	−10.87	202652.96	−1691.0
12	GP(t, s_y)	$B = c_0 + c_1 t + c_2 t^2$	3611.73	−8.80	202618.98	−1725.0

Appendix C
Transmission Spectrum Derived from Different Orbital Parameters

It has been shown that due to the limb-darkening effect, fixing impact parameter to imperfectly estimated values could introduce wavelength-dependent offsets to transmission spectrum in certain cases (Alexoudi et al. 2018, 2020). We have derived the values for i and $a/R_\star$ that are significantly different from the discovery paper (Hartman et al. 2016). To assess how

this would impact our derived transmission spectrum, we performed the same analyses for the white and spectroscopic light curves as we did in Section 3, except that we always held $i = 84°\!.2$ and $a/R_\star = 4.57$ fixed. Figure 6 presents the derived transmission spectrum based on Hartman et al.'s (2016) orbital parameters, which is consistent with our self-consistently derived transmission spectrum. We conclude that the orbital parameters (i and $a/R_\star$) are not the origin of the detected spectral signatures in our case.
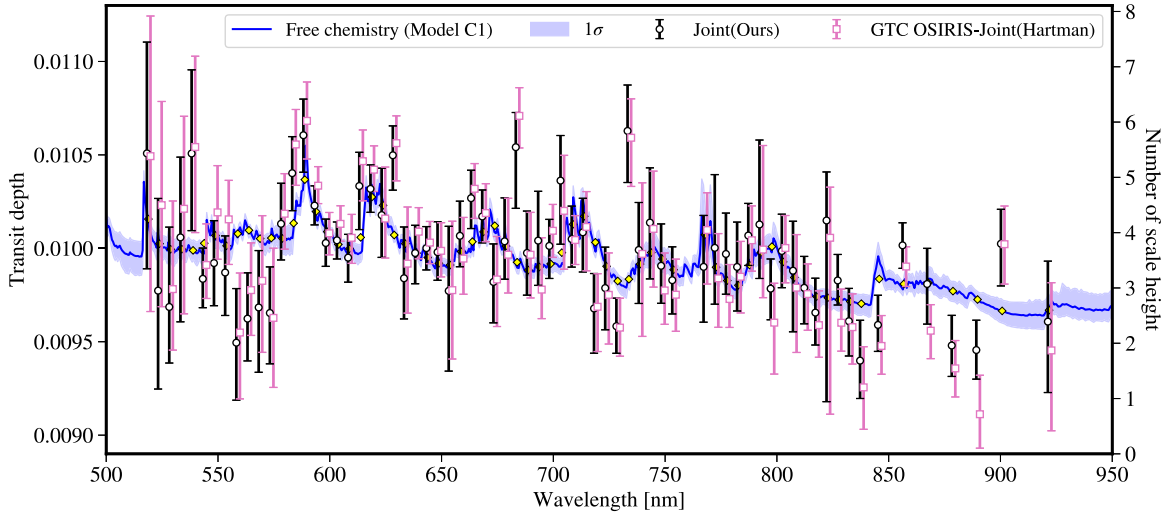
Figure 6. Comparison of transmission spectra based on different orbital parameters. Our transmission spectrum (black cicles) is self-consistent, with $i = 89°\!.10$ and $a/R_\star = 5.221$ determined from our white light curves. The other one (pink squares) is derived using $i = 84°\!.2$ and $a/R_\star = 4.57$ (Hartman et al. 2016). The two transmission spectra agree well with each other. The model spectrum is the same as the one shown in Figure 4.

Appendix D
Additional Tables and Figures

Table 3 presents the transmission spectra derived from the individual and joint light-curve analyses. Tables 4 and 5 give the parameters and statistics obtained in the spectral retrieval analyses performed on these individual and joint transmission spectra. Figure 7 shows the retrieved models and posterior distributions of planetary and stellar parameters assuming free-chemistry planetary atmosphere with stellar spots/faculae contamination. Figure 8 shows the stellar contaminations obtained in the retrieval analyses where both free-chemistry planetary atmosphere and stellar spots/faculae contamination are considered (i.e., Model D1 in Table 5).

Table 3
Transmission Spectrum of HAT-P-65b

λ (nm)	u_1 Prior	u_2 Prior	$R_p/R_\star$ (N1)	$R_p/R_\star$ (N2)	$R_p/R_\star$ (Joint)
517–522	$\mathcal{N}(0.526, 0.064^2)$	$\mathcal{N}(0.219, 0.048^2)$	$0.1043^{+0.0042}_{-0.0041}$	$0.0994^{+0.0051}_{-0.0062}$	$0.1025^{+0.0029}_{-0.0030}$
522–526	$\mathcal{N}(0.512, 0.060^2)$	$\mathcal{N}(0.237, 0.040^2)$	$0.1018^{+0.0038}_{-0.0036}$	$0.0952^{+0.0039}_{-0.0045}$	$0.0989^{+0.0025}_{-0.0027}$
527–532	$\mathcal{N}(0.499, 0.057^2)$	$\mathcal{N}(0.244, 0.037^2)$	$0.1040^{+0.0031}_{-0.0030}$	$0.0970^{+0.0015}_{-0.0014}$	$0.0984^{+0.0022}_{-0.0015}$
532–536	$\mathcal{N}(0.491, 0.058^2)$	$\mathcal{N}(0.247, 0.038^2)$	$0.0992^{+0.0029}_{-0.0027}$	$0.1013^{+0.0028}_{-0.0039}$	$0.1003^{+0.0021}_{-0.0023}$
537–542	$\mathcal{N}(0.485, 0.058^2)$	$\mathcal{N}(0.251, 0.038^2)$	$0.1070^{+0.0036}_{-0.0033}$	$0.0998^{+0.0024}_{-0.0024}$	$0.1025^{+0.0022}_{-0.0020}$
542–546	$\mathcal{N}(0.478, 0.059^2)$	$\mathcal{N}(0.256, 0.039^2)$	$0.1005^{+0.0031}_{-0.0031}$	$0.0991^{+0.0009}_{-0.0009}$	$0.0992^{+0.0008}_{-0.0008}$
547–552	$\mathcal{N}(0.477, 0.056^2)$	$\mathcal{N}(0.252, 0.037^2)$	$0.1044^{+0.0033}_{-0.0032}$	$0.0987^{+0.0011}_{-0.0017}$	$0.0996^{+0.0011}_{-0.0011}$
552–556	$\mathcal{N}(0.467, 0.056^2)$	$\mathcal{N}(0.258, 0.036^2)$	$0.0981^{+0.0024}_{-0.0028}$	$0.0997^{+0.0012}_{-0.0015}$	$0.0994^{+0.0010}_{-0.0012}$
557–562	$\mathcal{N}(0.458, 0.056^2)$	$\mathcal{N}(0.261, 0.036^2)$	$0.0979^{+0.0030}_{-0.0029}$	$0.0970^{+0.0019}_{-0.0022}$	$0.0974^{+0.0015}_{-0.0016}$
562–566	$\mathcal{N}(0.456, 0.055^2)$	$\mathcal{N}(0.261, 0.035^2)$	$0.1007^{+0.0035}_{-0.0044}$	$0.0979^{+0.0012}_{-0.0012}$	$0.0981^{+0.0012}_{-0.0012}$
566–571	$\mathcal{N}(0.449, 0.052^2)$	$\mathcal{N}(0.263, 0.032^2)$	$0.0960^{+0.0028}_{-0.0027}$	$0.0994^{+0.0016}_{-0.0018}$	$0.0984^{+0.0015}_{-0.0018}$
572–576	$\mathcal{N}(0.441, 0.054^2)$	$\mathcal{N}(0.271, 0.033^2)$	$0.0977^{+0.0017}_{-0.0024}$	$0.0990^{+0.0019}_{-0.0024}$	$0.0983^{+0.0013}_{-0.0014}$
576–581	$\mathcal{N}(0.439, 0.053^2)$	$\mathcal{N}(0.268, 0.033^2)$	$0.0984^{+0.0031}_{-0.0032}$	$0.1011^{+0.0016}_{-0.0011}$	$0.1007^{+0.0011}_{-0.0010}$
582–586	$\mathcal{N}(0.428, 0.053^2)$	$\mathcal{N}(0.276, 0.032^2)$	$0.1070^{+0.0050}_{-0.0068}$	$0.1019^{+0.0009}_{-0.0010}$	$0.1020^{+0.0010}_{-0.0010}$
586–591	$\mathcal{N}(0.428, 0.055^2)$	$\mathcal{N}(0.269, 0.035^2)$	$0.0997^{+0.0016}_{-0.0018}$	$0.1042^{+0.0015}_{-0.0011}$	$0.1030^{+0.0009}_{-0.0010}$
592–596	$\mathcal{N}(0.420, 0.052^2)$	$\mathcal{N}(0.277, 0.032^2)$	$0.1004^{+0.0008}_{-0.0008}$	$0.1017^{+0.0007}_{-0.0007}$	$0.1011^{+0.0005}_{-0.0005}$
596–601	$\mathcal{N}(0.413, 0.052^2)$	$\mathcal{N}(0.278, 0.031^2)$	$0.0996^{+0.0008}_{-0.0008}$	$0.1005^{+0.0011}_{-0.0011}$	$0.1001^{+0.0006}_{-0.0006}$
602–606	$\mathcal{N}(0.407, 0.051^2)$	$\mathcal{N}(0.281, 0.030^2)$	$0.0995^{+0.0007}_{-0.0008}$	$0.1006^{+0.0006}_{-0.0006}$	$0.1002^{+0.0005}_{-0.0005}$
606–611	$\mathcal{N}(0.407, 0.050^2)$	$\mathcal{N}(0.277, 0.030^2)$	$0.0979^{+0.0013}_{-0.0017}$	$0.1004^{+0.0007}_{-0.0007}$	$0.0998^{+0.0006}_{-0.0007}$
612–616	$\mathcal{N}(0.401, 0.050^2)$	$\mathcal{N}(0.273, 0.030^2)$	$0.1002^{+0.0041}_{-0.0017}$	$0.1020^{+0.0009}_{-0.0009}$	$0.1017^{+0.0009}_{-0.0011}$
616–621	$\mathcal{N}(0.397, 0.050^2)$	$\mathcal{N}(0.277, 0.030^2)$	$0.1020^{+0.0014}_{-0.0013}$	$0.1014^{+0.0008}_{-0.0008}$	$0.1016^{+0.0006}_{-0.0006}$
622–626	$\mathcal{N}(0.394, 0.049^2)$	$\mathcal{N}(0.276, 0.028^2)$	$0.1007^{+0.0017}_{-0.0017}$	$0.1013^{+0.0018}_{-0.0016}$	$0.1009^{+0.0012}_{-0.0011}$
626–632	$\mathcal{N}(0.389, 0.050^2)$	$\mathcal{N}(0.280, 0.029^2)$	$0.0952^{+0.0024}_{-0.0025}$	$0.1030^{+0.0007}_{-0.0008}$	$0.1025^{+0.0008}_{-0.0009}$
632–636	$\mathcal{N}(0.385, 0.049^2)$	$\mathcal{N}(0.279, 0.029^2)$	$0.1002^{+0.0020}_{-0.0020}$	$0.0989^{+0.0016}_{-0.0013}$	$0.0992^{+0.0014}_{-0.0011}$
637–642	$\mathcal{N}(0.380, 0.049^2)$	$\mathcal{N}(0.281, 0.029^2)$	$0.0977^{+0.0023}_{-0.0025}$	$0.1002^{+0.0007}_{-0.0009}$	$0.0999^{+0.0007}_{-0.0008}$
642–646	$\mathcal{N}(0.373, 0.049^2)$	$\mathcal{N}(0.283, 0.029^2)$	$0.1006^{+0.0018}_{-0.0019}$	$0.1001^{+0.0006}_{-0.0006}$	$0.1000^{+0.0006}_{-0.0006}$
647–652	$\mathcal{N}(0.366, 0.049^2)$	$\mathcal{N}(0.286, 0.028^2)$	$0.0979^{+0.0023}_{-0.0025}$	$0.1002^{+0.0009}_{-0.0008}$	$0.0999^{+0.0008}_{-0.0008}$
652–656	$\mathcal{N}(0.320, 0.053^2)$	$\mathcal{N}(0.315, 0.029^2)$	$0.0953^{+0.0028}_{-0.0028}$	$0.1002^{+0.0013}_{-0.0013}$	$0.0989^{+0.0017}_{-0.0022}$
657–662	$\mathcal{N}(0.311, 0.051^2)$	$\mathcal{N}(0.314, 0.026^2)$	$0.1003^{+0.0015}_{-0.0017}$	$0.1005^{+0.0017}_{-0.0012}$	$0.1003^{+0.0009}_{-0.0008}$
662–666	$\mathcal{N}(0.359, 0.048^2)$	$\mathcal{N}(0.286, 0.028^2)$	$0.1007^{+0.0040}_{-0.0037}$	$0.1013^{+0.0007}_{-0.0008}$	$0.1013^{+0.0007}_{-0.0008}$
667–672	$\mathcal{N}(0.358, 0.048^2)$	$\mathcal{N}(0.283, 0.028^2)$	$0.1000^{+0.0014}_{-0.0014}$	$0.1011^{+0.0008}_{-0.0008}$	$0.1008^{+0.0008}_{-0.0007}$
672–676	$\mathcal{N}(0.356, 0.045^2)$	$\mathcal{N}(0.282, 0.026^2)$	$0.0963^{+0.0022}_{-0.0026}$	$0.1001^{+0.0013}_{-0.0012}$	$0.0991^{+0.0010}_{-0.0011}$
677–682	$\mathcal{N}(0.354, 0.045^2)$	$\mathcal{N}(0.281, 0.026^2)$	$0.1009^{+0.0011}_{-0.0014}$	$0.0996^{+0.0013}_{-0.0010}$	$0.1002^{+0.0012}_{-0.0010}$
682–686	$\mathcal{N}(0.350, 0.044^2)$	$\mathcal{N}(0.281, 0.025^2)$	$0.0948^{+0.0041}_{-0.0037}$	$0.1034^{+0.0010}_{-0.0010}$	$0.1027^{+0.0009}_{-0.0016}$
686–691	$\mathcal{N}(0.347, 0.044^2)$	$\mathcal{N}(0.281, 0.025^2)$	$0.1004^{+0.0010}_{-0.0011}$	$0.0989^{+0.0012}_{-0.0010}$	$0.0999^{+0.0011}_{-0.0011}$
692–696	$\mathcal{N}(0.344, 0.045^2)$	$\mathcal{N}(0.281, 0.025^2)$	$0.1012^{+0.0014}_{-0.0027}$	$0.0998^{+0.0013}_{-0.0011}$	$0.1002^{+0.0013}_{-0.0012}$
696–701	$\mathcal{N}(0.342, 0.045^2)$	$\mathcal{N}(0.280, 0.025^2)$	$0.0970^{+0.0016}_{-0.0019}$	$0.1008^{+0.0007}_{-0.0007}$	$0.1001^{+0.0007}_{-0.0009}$
702–706	$\mathcal{N}(0.339, 0.044^2)$	$\mathcal{N}(0.280, 0.025^2)$	$0.1034^{+0.0010}_{-0.0011}$	$0.0990^{+0.0016}_{-0.0016}$	$0.1018^{+0.0012}_{-0.0017}$
706–711	$\mathcal{N}(0.334, 0.045^2)$	$\mathcal{N}(0.281, 0.025^2)$	$0.1020^{+0.0012}_{-0.0013}$	$0.0996^{+0.0007}_{-0.0008}$	$0.1002^{+0.0009}_{-0.0007}$
712–716	$\mathcal{N}(0.331, 0.045^2)$	$\mathcal{N}(0.281, 0.025^2)$	$0.1000^{+0.0015}_{-0.0016}$	$0.1007^{+0.0011}_{-0.0014}$	$0.1004^{+0.0009}_{-0.0011}$
716–721	$\mathcal{N}(0.329, 0.043^2)$	$\mathcal{N}(0.278, 0.024^2)$	$0.0970^{+0.0021}_{-0.0016}$	$0.0988^{+0.0010}_{-0.0012}$	$0.0984^{+0.0010}_{-0.0012}$
722–726	$\mathcal{N}(0.325, 0.044^2)$	$\mathcal{N}(0.281, 0.024^2)$	$0.0961^{+0.0022}_{-0.0024}$	$0.0999^{+0.0013}_{-0.0013}$	$0.0989^{+0.0011}_{-0.0011}$
726–731	$\mathcal{N}(0.323, 0.043^2)$	$\mathcal{N}(0.279, 0.024^2)$	$0.0978^{+0.0009}_{-0.0009}$	$0.0975^{+0.0016}_{-0.0017}$	$0.0979^{+0.0008}_{-0.0007}$
732–736	$\mathcal{N}(0.321, 0.043^2)$	$\mathcal{N}(0.281, 0.024^2)$	$0.1039^{+0.0013}_{-0.0014}$	$0.1008^{+0.0023}_{-0.0024}$	$0.1031^{+0.0012}_{-0.0013}$
736–741	$\mathcal{N}(0.317, 0.040^2)$	$\mathcal{N}(0.277, 0.022^2)$	$0.1014^{+0.0025}_{-0.0032}$	$0.0994^{+0.0014}_{-0.0017}$	$0.1000^{+0.0013}_{-0.0014}$
742–746	$\mathcal{N}(0.313, 0.041^2)$	$\mathcal{N}(0.279, 0.022^2)$	$0.1022^{+0.0011}_{-0.0013}$	$0.0988^{+0.0012}_{-0.0010}$	$0.1007^{+0.0015}_{-0.0015}$
746–752	$\mathcal{N}(0.310, 0.042^2)$	$\mathcal{N}(0.281, 0.023^2)$	$0.1002^{+0.0014}_{-0.0012}$	$0.0992^{+0.0027}_{-0.0016}$	$0.0995^{+0.0011}_{-0.0010}$
752–756	$\mathcal{N}(0.308, 0.042^2)$	$\mathcal{N}(0.282, 0.023^2)$	$0.0981^{+0.0021}_{-0.0020}$	$0.0993^{+0.0011}_{-0.0011}$	$0.0991^{+0.0009}_{-0.0009}$
766–770	$\mathcal{N}(0.298, 0.041^2)$	$\mathcal{N}(0.281, 0.022^2)$	$0.1016^{+0.0011}_{-0.0023}$	$0.0986^{+0.0013}_{-0.0013}$	$0.0995^{+0.0014}_{-0.0015}$
771–776	$\mathcal{N}(0.297, 0.039^2)$	$\mathcal{N}(0.280, 0.021^2)$	$0.1009^{+0.0023}_{-0.0033}$	$0.0997^{+0.0021}_{-0.0017}$	$0.1000^{+0.0020}_{-0.0015}$

Table 3
(Continued)

λ (nm)	u_1 Prior	u_2 Prior	$R_p/R_\star$ (N1)	$R_p/R_\star$ (N2)	$R_p/R_\star$ (Joint)
776–780	$\mathcal{N}(0.293, 0.039^2)$	$\mathcal{N}(0.282, 0.020^2)$	$0.1045^{+0.0023}_{-0.0022}$	$0.0986^{+0.0011}_{-0.0013}$	$0.0998^{+0.0011}_{-0.0011}$
781–786	$\mathcal{N}(0.292, 0.038^2)$	$\mathcal{N}(0.280, 0.020^2)$	$0.1016^{+0.0012}_{-0.0013}$	$0.0979^{+0.0013}_{-0.0015}$	$0.0995^{+0.0012}_{-0.0012}$
786–790	$\mathcal{N}(0.291, 0.041^2)$	$\mathcal{N}(0.283, 0.021^2)$	$0.1021^{+0.0016}_{-0.0014}$	$0.0993^{+0.0009}_{-0.0008}$	$0.1003^{+0.0009}_{-0.0008}$
791–796	$\mathcal{N}(0.289, 0.041^2)$	$\mathcal{N}(0.281, 0.022^2)$	$0.1016^{+0.0028}_{-0.0023}$	$0.1003^{+0.0034}_{-0.0017}$	$0.1006^{+0.0022}_{-0.0014}$
796–800	$\mathcal{N}(0.288, 0.041^2)$	$\mathcal{N}(0.282, 0.022^2)$	$0.1064^{+0.0038}_{-0.0042}$	$0.0984^{+0.0008}_{-0.0010}$	$0.0989^{+0.0008}_{-0.0008}$
801–806	$\mathcal{N}(0.285, 0.041^2)$	$\mathcal{N}(0.281, 0.022^2)$	$0.0995^{+0.0018}_{-0.0023}$	$0.1001^{+0.0011}_{-0.0012}$	$0.0999^{+0.0010}_{-0.0012}$
806–810	$\mathcal{N}(0.285, 0.041^2)$	$\mathcal{N}(0.280, 0.022^2)$	$0.1003^{+0.0017}_{-0.0022}$	$0.0976^{+0.0023}_{-0.0029}$	$0.0994^{+0.0013}_{-0.0016}$
810–815	$\mathcal{N}(0.283, 0.043^2)$	$\mathcal{N}(0.282, 0.024^2)$	$0.0989^{+0.0013}_{-0.0014}$	$0.0986^{+0.0013}_{-0.0017}$	$0.0989^{+0.0009}_{-0.0010}$
816–820	$\mathcal{N}(0.278, 0.041^2)$	$\mathcal{N}(0.280, 0.022^2)$	$0.0969^{+0.0024}_{-0.0021}$	$0.0985^{+0.0013}_{-0.0010}$	$0.0983^{+0.0009}_{-0.0009}$
820–825	$\mathcal{N}(0.275, 0.039^2)$	$\mathcal{N}(0.279, 0.021^2)$	$0.0950^{+0.0009}_{-0.0009}$	$0.1022^{+0.0009}_{-0.0009}$	$0.1007^{+0.0013}_{-0.0048}$
826–830	$\mathcal{N}(0.275, 0.039^2)$	$\mathcal{N}(0.281, 0.021^2)$	$0.0984^{+0.0024}_{-0.0019}$	$0.0990^{+0.0008}_{-0.0007}$	$0.0991^{+0.0007}_{-0.0007}$
830–835	$\mathcal{N}(0.274, 0.040^2)$	$\mathcal{N}(0.278, 0.021^2)$	$0.0982^{+0.0010}_{-0.0011}$	$0.0970^{+0.0019}_{-0.0021}$	$0.0980^{+0.0009}_{-0.0009}$
836–840	$\mathcal{N}(0.272, 0.039^2)$	$\mathcal{N}(0.278, 0.021^2)$	$0.0965^{+0.0012}_{-0.0012}$	$0.0993^{+0.0030}_{-0.0028}$	$0.0969^{+0.0011}_{-0.0010}$
840–851	$\mathcal{N}(0.264, 0.039^2)$	$\mathcal{N}(0.281, 0.020^2)$	$0.0994^{+0.0024}_{-0.0020}$	$0.0976^{+0.0009}_{-0.0009}$	$0.0979^{+0.0008}_{-0.0007}$
852–862	$\mathcal{N}(0.258, 0.039^2)$	$\mathcal{N}(0.281, 0.020^2)$	$0.1001^{+0.0007}_{-0.0007}$	$0.0998^{+0.0019}_{-0.0018}$	$0.1001^{+0.0006}_{-0.0006}$
862–874	$\mathcal{N}(0.247, 0.032^2)$	$\mathcal{N}(0.271, 0.015^2)$	$0.0990^{+0.0019}_{-0.0019}$	$0.0988^{+0.0012}_{-0.0015}$	$0.0990^{+0.0010}_{-0.0011}$
874–884	$\mathcal{N}(0.253, 0.037^2)$	$\mathcal{N}(0.280, 0.019^2)$	$0.0975^{+0.0020}_{-0.0015}$	$0.0973^{+0.0010}_{-0.0011}$	$0.0974^{+0.0008}_{-0.0009}$
885–896	$\mathcal{N}(0.256, 0.037^2)$	$\mathcal{N}(0.279, 0.019^2)$	$0.0972^{+0.0010}_{-0.0010}$	$0.0974^{+0.0017}_{-0.0018}$	$0.0972^{+0.0008}_{-0.0008}$
896–906	$\mathcal{N}(0.245, 0.033^2)$	$\mathcal{N}(0.271, 0.016^2)$	$0.0982^{+0.0035}_{-0.0032}$	$0.1004^{+0.0011}_{-0.0012}$	$0.1001^{+0.0009}_{-0.0011}$
907–938	$\mathcal{N}(0.248, 0.037^2)$	$\mathcal{N}(0.281, 0.019^2)$	$0.0977^{+0.0028}_{-0.0030}$	$0.0977^{+0.0020}_{-0.0024}$	$0.0980^{+0.0017}_{-0.0019}$

Table 4
Parameter Estimation for Spectral Retrievals

| Parameter	Prior	Posterior Estimate		
		2018 Jul 29	2020 Aug 7	Joint
Retrieval assuming equilibrium chemistry				
T–P $\log \delta\,(\mathrm{bar}^{-1})$	$\mathcal{N}(-5.5, 2.5^2)$	$-6.6^{+1.3}_{-1.8}$	$-6.4^{+1.8}_{-1.7}$	$-6.1^{+1.4}_{-1.6}$
T–P $\log \gamma$	$\mathcal{N}(0, 2^2)$	$-1.4^{+0.9}_{-1.2}$	$-0.9^{+1.2}_{-1.4}$	$-1.0^{+1.1}_{-1.2}$
T–P $T_{int}(K)$	$\mathcal{U}(0, 1500)$	974^{+351}_{-467}	895^{+378}_{-477}	789^{+415}_{-430}
T–P $T_{eq}(K)$	$\mathcal{U}(0, 4000)$	1612^{+84}_{-191}	1774^{+339}_{-370}	1645^{+255}_{-244}
T–P $\log P_{trans}(bar)$	$\mathcal{N}(-3, 3^2)$	$-5.1^{+1.4}_{-1.0}$	$-3.9^{+2.4}_{-2.2}$	$-3.8^{+1.9}_{-1.9}$
T–P α	$\mathcal{N}(0.25, 0.4^2)$	$0.35^{+0.28}_{-0.21}$	$0.26^{+0.28}_{-0.28}$	$0.26^{+0.27}_{-0.29}$
$\log P_0(bar)$	$\mathcal{U}(-4, 2)$	$-3.7^{+0.3}_{-0.2}$	$-3.6^{+0.4}_{-0.2}$	$-3.5^{+0.5}_{-0.3}$
$\log P_{cloud}(bar)$	$\mathcal{U}(-4, 2)$	$-0.5^{+1.5}_{-1.7}$	$-1.2^{+1.7}_{-1.4}$	$-1.6^{+1.8}_{-1.5}$
$\log A_{RS}$	$\mathcal{U}(0, 4)$	$1.2^{+0.8}_{-0.7}$	$1.6^{+1.0}_{-0.9}$	$1.7^{+0.9}_{-0.8}$
C/O	$\mathcal{U}(0.05, 2)$	$0.7^{+0.1}_{-0.2}$	$1.4^{+0.3}_{-0.3}$	$1.2^{+0.4}_{-0.6}$
$\log Z$	$\mathcal{U}(-2, 3)$	$0.4^{+0.6}_{-0.9}$	$0.9^{+0.6}_{-1.3}$	$0.0^{+1.1}_{-1.4}$
ϕ	$\mathcal{U}(0, 1)$	$0.37^{+0.32}_{-0.25}$	$0.37^{+0.24}_{-0.19}$	$0.36^{+0.23}_{-0.17}$
Retrieval assuming free chemistry				
T–P $T_{iso}(K)$	$\mathcal{U}(800, 3000)$	1170^{+266}_{-233}	2410^{+402}_{-614}	1018^{+225}_{-138}
$\log P_0(bar)$	$\mathcal{U}(-4, 2)$	$-3.3^{+0.7}_{-0.4}$	$-3.6^{+0.4}_{-0.3}$	$-3.4^{+0.6}_{-0.4}$
$\log P_{cloud}(bar)$	$\mathcal{U}(-4, 2)$	$0.5^{+1.0}_{-1.1}$	$-2.7^{+0.5}_{-0.3}$	$0.2^{+1.2}_{-1.3}$
$\log A_{RS}$	$\mathcal{U}(-2, 4)$	$-0.4^{+1.0}_{-1.0}$	$-0.4^{+1.0}_{-1.0}$	$0.3^{+0.7}_{-1.0}$
$\log X_{TiO}$	$\mathcal{U}(-10, 0)$	$-8.5^{+0.6}_{-0.8}$	$-7.4^{+0.3}_{-0.5}$	$-8.2^{+0.5}_{-0.6}$
$\log X_{VO}$	$\mathcal{U}(-10, 0)$	$-7.9^{+0.6}_{-0.7}$	$-9.1^{+0.7}_{-0.6}$	$-8.5^{+0.5}_{-0.7}$
$\log X_{Na}$	$\mathcal{U}(-10, 0)$	$-8.0^{+1.5}_{-1.3}$	$-3.3^{+0.7}_{-1.1}$	$-5.6^{+1.1}_{-1.7}$
$\log X_{K}$	$\mathcal{U}(-10, 0)$	$-6.5^{+1.6}_{-1.5}$	$-8.2^{+1.4}_{-1.2}$	$-8.1^{+1.4}_{-1.2}$
$\log X_{H_2O}$	$\mathcal{U}(-10, 0)$	$-6.8^{+2.1}_{-2.2}$	$-6.0^{+2.7}_{-2.7}$	$-6.4^{+2.5}_{-2.3}$
Retrieval assuming free chemistry with spots/faculae contamination				
T–P $T_{iso}(K)$	$\mathcal{U}(800, 3000)$	1241^{+245}_{-239}	1900^{+545}_{-341}	1091^{+224}_{-166}
$\log P_0(bar)$	$\mathcal{U}(-4, 2)$	$-3.5^{+0.6}_{-0.3}$	$-3.1^{+0.8}_{-0.5}$	$-3.0^{+0.8}_{-0.6}$

Table 4
(Continued)

Parameter	Prior	Posterior Estimate		
		2018 Jul 29	2020 Aug 7	Joint
$\log P_{\rm cloud}({\rm bar})$	$\mathcal{U}(-4, 2)$	$0.5^{+1.0}_{-1.0}$	$-0.6^{+1.3}_{-1.2}$	$0.0^{+1.1}_{-1.2}$
$\log A_{\rm RS}$	$\mathcal{U}(-2, 4)$	$-0.6^{+0.9}_{-0.8}$	$0.2^{+1.2}_{-1.1}$	$0.2^{+0.9}_{-1.1}$
$\log X_{\rm TiO}$	$\mathcal{U}(-10, 0)$	$-8.8^{+0.8}_{-0.6}$	$-7.7^{+0.7}_{-0.9}$	$-7.7^{+0.6}_{-0.7}$
$\log X_{\rm VO}$	$\mathcal{U}(-10, 0)$	$-8.2^{+0.7}_{-0.5}$	$-9.0^{+0.7}_{-0.6}$	$-8.4^{+0.7}_{-0.7}$
$\log X_{\rm Na}$	$\mathcal{U}(-10, 0)$	$-8.2^{+1.6}_{-1.2}$	$-1.0^{+0.5}_{-0.9}$	$-2.5^{+1.3}_{-1.5}$
$\log X_{\rm K}$	$\mathcal{U}(-10, 0)$	$-6.8^{+1.4}_{-1.1}$	$-8.0^{+1.4}_{-1.2}$	$-7.7^{+1.6}_{-1.3}$
$\log X_{\rm H_2O}$	$\mathcal{U}(-10, 0)$	$-6.7^{+1.8}_{-2.0}$	$-5.8^{+2.4}_{-2.3}$	$-5.9^{+2.3}_{-2.4}$
$T_{\rm spot}({\rm K})$	$\mathcal{U}(2000, 5835)$	5358^{+290}_{-639}	4292^{+867}_{-656}	4930^{+508}_{-888}
$f_{\rm spot}$	$\mathcal{U}(0, 1)$	$0.15^{+0.23}_{-0.10}$	$0.13^{+0.10}_{-0.07}$	$0.10^{+0.15}_{-0.06}$
$T_{\rm faculae}({\rm K})$	$\mathcal{U}(5835, 7000)$	5997^{+214}_{-107}	6257^{+251}_{-128}	6116^{+134}_{-102}
$f_{\rm faculae}$	$\mathcal{U}(0, 1)$	$0.25^{+0.35}_{-0.17}$	$0.50^{+0.24}_{-0.20}$	$0.53^{+0.23}_{-0.19}$

Table 5
Statistics from Bayesian Spectral Retrieval Analysis

#	Model	dof	2018 Jul 29				2020 Aug 7				Joint			
			$\chi^2_{\rm MAP}$ [a]	$\ln\mathcal{Z}$	$\Delta\ln\mathcal{Z}$	FS[b]	$\chi^2_{\rm MAP}$ [a]	$\ln\mathcal{Z}$	$\Delta\ln\mathcal{Z}$	FS[b]	$\chi^2_{\rm MAP}$ [a]	$\ln\mathcal{Z}$	$\Delta\ln\mathcal{Z}$	FS[b]
A. Simple assumption														
1	Flat line	69	135.4	410.98	−0.3	N/A	132.1	442.09	−6.9	4.1σ	127.7	456.23	−10.0	4.8σ
2	Sloped line	68	127.8	411.25	0	Ref.	111.1	448.94	0	Ref.	99.1	466.20	0	Ref.
B. Retrieval assuming equilibrium chemistry														
1	Full model	58	107.1	419.05	0	Ref.	93.2	457.82	0	Ref.	77.9	475.79	0	Ref.
C. Retrieval assuming free chemistry														
1	Full model	61	103.1	423.22	0	Ref.	83.8	459.48	0	Ref.	76.6	476.34	0	Ref.
2	No TiO	60	109.9	421.12	−2.1	2.6σ	94.9	455.62	−3.9	3.3σ	89.2	471.14	−5.2	3.7σ
3	No VO	60	115.1	418.49	−4.7	3.5σ	84.0	460.78	1.3	-2.2σ	81.9	475.41	−0.9	2.0σ
4	No Na	60	102.4	423.96	0.7	N/A	92.3	456.26	−3.2	3.0σ	79.5	475.18	−1.2	2.1σ
5	No K	60	105.2	422.03	−1.2	2.1σ	83.8	460.05	0.6	N/A	76.8	477.05	0.7	N/A
6	No H₂O	60	102.4	423.60	0.4	N/A	84.1	458.82	−0.7	N/A	76.4	476.04	−0.3	N/A
7	No TiO+Na	59	110.1	421.68	−1.5	2.3σ	112.7	449.50	−10.0	4.8σ	98.8	468.08	−8.3	4.5σ
D. Retrieval assuming spots/faculae contamination														
1	C1 with spots/faculae	57	99.6	420.70	0	Ref.	72.7	463.09	0	Ref.	73.9	474.98	0	Ref.
2	Spots/faculae only	65	106.7	417.84	−2.9	2.9σ	93.4	457.08	−6.0	3.9σ	86.4	471.97	−3.0	3.0σ

[a] χ^2 for the maximum a posteriori (MAP) model.
[b] The Bayes factor $B_{10} = \mathcal{Z}_1/\mathcal{Z}_0$, or $\ln B_{10} = \Delta\ln\mathcal{Z}$, was converted to frequentist significance (FS) following Trotta (2008) and Benneke & Seager (2013). It is labeled as N/A if $|\Delta\ln\mathcal{Z}| < 0.9$. The number of "sigmas" is a useful frequentist metric to express the odds in favor of a more complex model, which does not necessarily mean the detection of a species in the spectrum of a planet (Welbanks & Madhusudhan 2021).
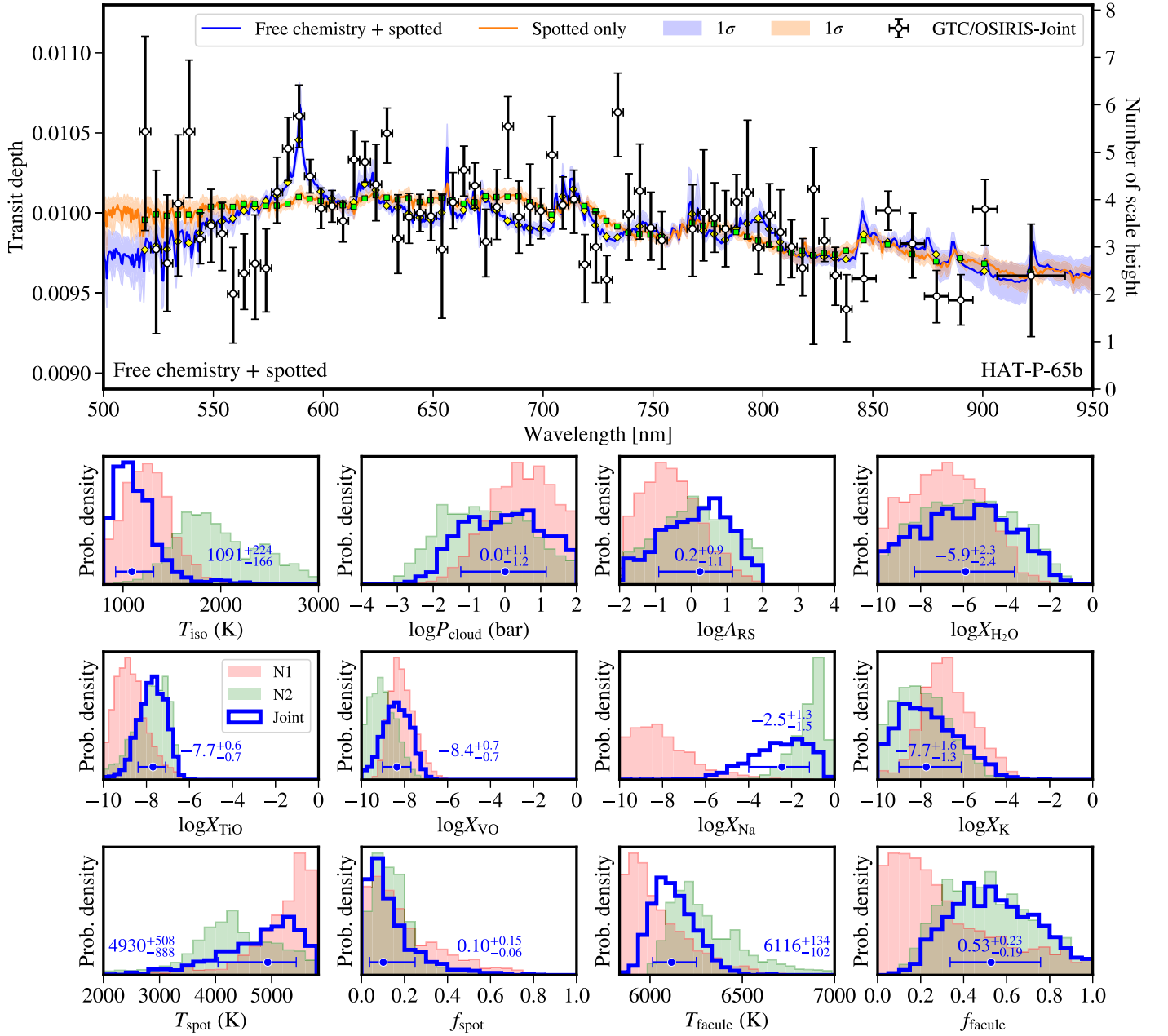
Figure 7. Transmission spectrum of HAT-P-65b and retrieved atmospheric properties assuming free chemistry along with contamination from spots and faculae. The first row presents the jointly derived transmission spectrum (white circles) and retrieved models (blue line and shaded areas). For comparison, we show the best model from another retrieval analysis where only spots/faculae contamination is used to fit the data (orange line and shaded areas). The second to fourth rows present the retrieved planetary atmosphere properties (see the description in Figure 4) and stellar spots/faculae properties (temperatures $T_{\rm spot}$, $T_{\rm faculae}$ and fractions $f_{\rm spot}$, $f_{\rm faculae}$). The blue, red, and green lines and shaded areas refer to the retrieval results based on the joint, Night 1 (N1), and Night 2 (N2) transmission spectra, respectively.
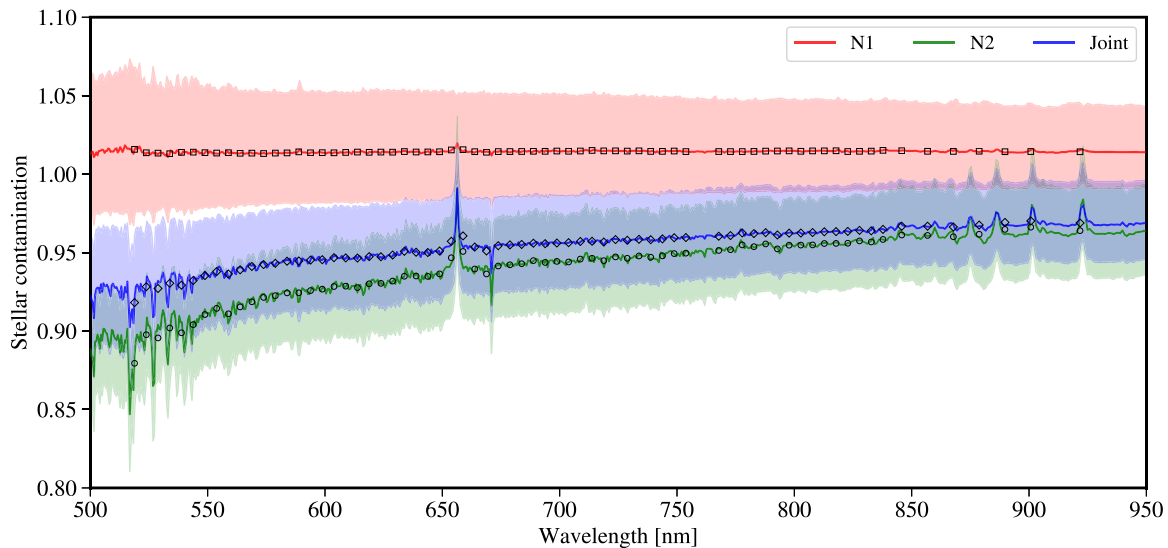
Figure 8. Stellar contaminations obtained in the retrieval analyses assuming free-chemistry with spots/faculae (see Figure 7), for Night 1 (N1, red), Night 2 (N2, green), and joint (blue) transmission spectra, respectively. The spectral signatures observed at ∼585–598 nm and ∼615–628 nm in the transmission spectra cannot be explained by these contaminations.

ORCID iDs

Guo Chen ⬥ https://orcid.org/0000-0003-0740-5433
Enric Pallé ⬥ https://orcid.org/0000-0003-0987-1593
Hannu Parviainen ⬥ https://orcid.org/0000-0001-5519-1391
Felipe Murgas ⬥ https://orcid.org/0000-0001-9087-1245
Fei Yan ⬥ https://orcid.org/0000-0001-9585-9034

References

Alexoudi, X., Mallonn, M., Keles, E., et al. 2020, A&A, 640, A134
Alexoudi, X., Mallonn, M., von Essen, C., et al. 2018, A&A, 620, A142
Ambikasaran, S., Foreman-Mackey, D., Greengard, L., Hogg, D. W., & O'Neil, M. 2015, ITPAM, 38, 252
Arcangeli, J., Désert, J.-M., Line, M. R., et al. 2018, ApJL, 855, L30
Benneke, B., & Seager, S. 2013, ApJ, 778, 153
Buchner, J., Georgakakis, A., Nandra, K., et al. 2014, A&A, 564, A125
Casasayas-Barris, N., Palle, E., Stangret, M., et al. 2021, A&A, 647, A26
Cepa, J., Aguiar, M., Escalera, V. G., et al. 2000, Proc. SPIE, 4008, 623
Chen, G., Casasayas-Barris, N., Pallé, E., et al. 2020a, A&A, 642, A54
Chen, G., Casasayas-Barris, N., Pallé, E., et al. 2020b, A&A, 635, A171
Chen, G., Pallé, E., Parviainen, H., et al. 2021, MNRAS, 500, 5420
Chen, G., Pallé, E., Welbanks, L., et al. 2018, A&A, 616, A145
Eastman, J., Siverd, R., & Gaudi, B. S. 2010, PASP, 122, 935
Ehrenreich, D., Lovis, C., Allart, R., et al. 2020, Natur, 580, 597
Espinoza, N., & Jordán, A. 2015, MNRAS, 450, 1879
Espinoza, N., Rackham, B. V., Jordán, A., et al. 2019, MNRAS, 482, 2065
Evans, T. M., Sing, D. K., Goyal, J. M., et al. 2018, AJ, 156, 283
Evans, T. M., Sing, D. K., Kataria, T., et al. 2017, Natur, 548, 58
Evans, T. M., Sing, D. K., Wakeford, H. R., et al. 2016, ApJL, 822, L4
Feroz, F., Hobson, M. P., & Bridges, M. 2009, MNRAS, 398, 1601
Foreman-Mackey, D., Hogg, D. W., Lang, D., & Goodman, J. 2013, PASP, 125, 306
Fortney, J. J., Lodders, K., Marley, M. S., & Freedman, R. S. 2008, ApJ, 678, 1419
Gibson, N. P., Aigrain, S., Roberts, S., et al. 2012, MNRAS, 419, 2683

Guillot, T. 2010, A&A, 520, A27
Hartman, J. D., Bakos, G. Á., Bhatti, W., et al. 2016, AJ, 152, 182
Haynes, K., Mandell, A. M., Madhusudhan, N., Deming, D., & Knutson, H. 2015, ApJ, 806, 146
Herman, M. K., de Mooij, E. J. W., Jayawardhana, R., & Brogi, M. 2020, AJ, 160, 93
Hubeny, I., Burrows, A., & Sudarsky, D. 2003, ApJ, 594, 1011
Hunter, J. D. 2007, CSE, 9, 90
Husser, T. O., Wende-von Berg, S., Dreizler, S., et al. 2013, A&A, 553, A6
Kirkpatrick, J. D., Reid, I. N., Liebert, J., et al. 1999, ApJ, 519, 802
Knutson, H. A., Howard, A. W., & Isaacson, H. 2010, ApJ, 720, 1569
Kreidberg, L. 2015, PASP, 127, 1161
Lecavelier Des Etangs, A., Pont, F., Vidal-Madjar, A., & Sing, D. 2008, A&A, 481, L83
Lothringer, J. D., Barman, T., & Koskinen, T. 2018, ApJ, 866, 27
MacDonald, R. J., & Madhusudhan, N. 2017, MNRAS, 469, 1979
Mandel, K., & Agol, E. 2002, ApJL, 580, L171
Mansfield, M., Bean, J. L., Line, M. R., et al. 2018, AJ, 156, 10
Merritt, S. R., Gibson, N. P., Nugroho, S. K., et al. 2020, A&A, 636, A117
Mollière, P., van Boekel, R., Bouwman, J., et al. 2017, A&A, 600, A10
Mollière, P., Wardenier, J. P., van Boekel, R., et al. 2019, A&A, 627, A67
Nugroho, S. K., Gibson, N. P., de Mooij, E. J. W., et al. 2020, ApJL, 898, L31
Nugroho, S. K., Kawahara, H., Masuda, K., et al. 2017, AJ, 154, 221
Ochsenbein, F., Bauer, P., & Marcout, J. 2000, A&AS, 143, 23
Parmentier, V., Line, M. R., Bean, J. L., et al. 2018, A&A, 617, A110
Parmentier, V., Showman, A. P., & Lian, Y. 2013, A&A, 558, A91
Pino, L., Désert, J.-M., Brogi, M., et al. 2020, ApJL, 894, L27
Rasmussen, C. E., & Williams, C. K. I. 2006, Gaussian Processes for Machine Learning (Cambridge, MA: The MIT Press)
Sedaghati, E., Boffin, H. M. J., MacDonald, R. J., et al. 2017, Natur, 549, 238
Serindag, D. B., Nugroho, S. K., Mollière, P., et al. 2021, A&A, 645, A90
Sheppard, K. B., Mandell, A. M., Tamburo, P., et al. 2017, ApJL, 850, L32
Spiegel, D. S., Silverio, K., & Burrows, A. 2009, ApJ, 699, 1487
Trotta, R. 2008, ConPh, 49, 71
Welbanks, L., & Madhusudhan, N. 2021, arXiv:2103.08600
Yan, F., Pallé, E., Reiners, A., et al. 2020, A&A, 640, L5